

RESEARCH ARTICLE

Isotope abundance ratio measurements using femtosecond laser ablation ionization mass spectrometry

Marek Tulej¹  | Anna Neubeck²  | Andreas Riedo¹  | Rustam Lukmanov¹ |
Valentine Grimaudo¹  | Niels F.W. Ligterink³  | Magnus Ivarsson^{4,5}  |
Wolfgang Bach⁶  | Coenraad de Koning¹  | Peter Wurz¹ 

¹Physics Institute, Space Research and Planetary Sciences, University of Bern, Bern, Switzerland

²Department of Geological Sciences, Uppsala University, Uppsala, Sweden

³Center for Space and Habitability, University of Bern, Bern, Switzerland

⁴Department of Biology, University of Southern Denmark, Odense, Denmark

⁵Department of Paleobiology, Swedish Museum of Natural History, Stockholm, Sweden

⁶Department of Geosciences, University of Bremen, Bremen, Germany

Correspondence

Marek Tulej, Physics Institute, Space Research and Planetary Sciences, University of Bern, Bern, Switzerland.

Email: marek.tulej@space.unibe.ch

Funding information

Swedish Research Council, Grant/Award Numbers: 2012-4364, 2017-04129, 2017-05018; Swiss National Science Foundation; Villum Investigator Grant to Don Canfield, Grant/Award Number: 16518

Abstract

Accurate isotope ratio measurements are of high importance in various scientific fields, ranging from radio isotope geochronology of solids to studies of element isotopes fractionated by living organisms. Instrument limitations, such as unresolved isobaric inferences in the mass spectra, or cosampling of the material of interest together with the matrix material may reduce the quality of isotope measurements. Here, we describe a method for accurate isotope ratio measurements using our laser ablation ionization time-of-flight mass spectrometer (LIMS) that is designed for in situ planetary research. The method is based on chemical depth profiling that allows for identifying micrometer scale inclusions embedded in surrounding rocks with different composition inside the bulk of the sample. The data used for precise isotope measurements are improved using a spectrum cleaning procedure that ensures removal of low quality spectra. Furthermore, correlation of isotopes of an element is used to identify and reject the data points that, for example, do not belong to the species of interest. The measurements were conducted using IR femtosecond laser irradiation focused on the sample surface to a spot size of $\sim 12 \mu\text{m}$. Material removal was conducted for a predefined number of laser shots, and time-of-flight mass spectra were recorded for each of the ablated layers. Measurements were conducted on NIST SRM 986 Ni isotope standard, trevorite mineral, and micrometer-sized inclusions embedded in aragonite. Our measurements demonstrate that element isotope ratios can be measured with accuracies and precision at the permille level, exemplified by the analysis of B, Mg, and Ni element isotopes. The method applied will be used for in situ investigation of samples on planetary surfaces, for accurate quantification of element fractionation induced by, for example, past or present life or by geochemical processes.

KEYWORDS

depth profiling, isotope ratio measurements, in situ chemical analysis, laser ablation ionization mass spectrometry, microfossils, miniature laser mass analyzer, time-of-flight mass spectrometry

1 | INTRODUCTION

To date, secondary ion mass spectrometry (SIMS, including nano-SIMS), laser ablation inductively coupled plasma mass spectrometry (LA ICP MS), and thermal ionization mass spectrometry (TIMS) are the state-of-the-art analytical measurement techniques for high-quality element isotope analysis of solid samples in the laboratory.¹ Typically, measurements on standard reference materials (SRM) are conducted in parallel of the unknown sample for true quantification of the measurement results. Resonance enhanced ionization mass spectrometry (RIMS) and atomic mass spectrometry (AMS) are more specific measurement techniques but offer high isotope selectivity and allow highly sensitive measurements of isotope ratios for elements down to ppb abundance. However, these methods usually involve application of complicated and bulky experimental equipment that definitely cannot be applied in space exploration where parameters such as volume, weight, and power consumption are highly limited. Among all these techniques, laser ablation ionization mass spectrometry (LIMS) is rarely applied for accurate element isotope ratio analysis due to its alleged low precision established by studies conducted with early LIMS instruments (e.g., LAMMA) equipped with nanosecond-laser ablation ion sources. In spite of the high detection sensitivity of LIMS instruments, element fractionation induced by laser ablation, its dependence on laser focus shape, wavelength, and polarization, on plasma variabilities, and matrix effects can limit the accuracy of element isotope ratio measurements.²

In recent years, LIMS has been equipped with femtosecond laser ablation ion sources. Improvements to stoichiometric elemental analysis have been reported by several groups.^{3–6} Using femtosecond lasers results in nonthermal material ablation that allows for a much more quantitative assessment of individual elements.⁷ Moreover, the application of femtosecond laser pulses limits thermal effects at the sample surface, which causes reduced sample damage compared to nanosecond laser radiation sources, and provides a better stoichiometric analysis of the elemental composition of the investigated solid.

Several frequently mentioned effects limiting the precision and accuracy of isotope measurements by ICP-MS using laser ablation are instrument mass bias, isobaric interferences, drift of mass scale, and matrix effects, which can also be pertinent for LIMS.⁸ LIMS measurements suffer mostly from plasma variabilities, as well as variations in ion intensities due to space charge in the ablated plume and surface charging. The space charge of the expanding ion plume (Coulombic repulsion) can cause the mass discrimination loss of the ion transmission and typically severely affect the mass resolution. Surface charging can also affect mass resolution and shapes of the mass peaks, such as broadening. Large ion intensity variation due to plasma variability can affect the performance of the detector system. Due to the dead time (detector saturation), typically observed when the counting rates exceed 10^6 s^{-1} in multichannel plate (MCP) ion detectors, true counting rates are underestimated.^{9,10} Another important consideration is the requirement for sufficiently high mass resolution. This can be important when a low abundant isotope peak is present in the immediate vicinity of a high abundant peak. Generally, when the mass

resolution is low, peak quantification cannot be accurately performed due to the overlap of the flanks of neighboring peaks. An important interference to the accuracy and precision of isotope measurements is the presence of isobaric interferences with the ions of interest in the mass spectra caused by cluster and molecular of the same integer mass. TOF LIMS instruments allowing mass resolutions ($m/\Delta m$) exceeding a few thousand were developed and can be used to resolve isobaric interferences.^{5,11} Alternatively, the reduction of the clusters and molecular ions from the ablated ions has been demonstrated by using a helium-filled collision cell for the ablated material in a laboratory LIMS system.^{12,13} Very recently, using a double pulse laser ablation/ionization method demonstrated the reduction of cluster and molecular contributions in the recorded mass spectra.¹⁴ Above discussed effects, ranging from interferences by cluster and molecular contributions to charge effects, will limit even more severely the accuracy of isotope measurements conducted by miniature mass analyzers or small and portable instruments for field research.

Precise measurement of isotope ratios is required for various research and application fields. Among the 1,700 isotopes, only 264 element isotopes are stable. Nevertheless, their abundances can undergo fine changes due to nuclear, biological, chemical, geochemical, and physical processes. The measure of these fine variations provides information on the source of these variations. In our long-term goal of developing the laser ablation ionization mass spectrometer for in situ investigation of solids on planetary surfaces, improvements of the instrument performance to measure the isotope variation accurately and precisely are one of the most important tasks. In situ isotope analysis of solids on planetary surfaces can contribute to geochemistry and geochronology of rocks. There are few miniature TOF MS systems using a laser ablation which serve as prototype space instruments.^{15–19} Only two of them have demonstrated capabilities accurate and precise isotope measurements at this time.^{18,20} One of the instruments uses a resonant ionization of neutral material from laser ablation and demonstrated dating of rocks using Sr/Rb dating method.¹⁸ In previous studies, we demonstrated the capability to measure the Pb isotope abundance with high accuracy and precision, which is important for dating using the Pb/Pb method, with our miniature laser ablation ionization mass spectrometer by applying UV-nanosecond laser irradiation as ablation and ionization source.²⁰ Obviously, quantitative isotope analyses for a larger number of elements would be of considerable interest to dating applications on the planetary surfaces, such as Rb/Sr, U/Pb, or Re/Os. Additionally, one can infer geological processes during formation and transport of minerals, wash out processes, weathering, and cosmogenic effects from quantitative isotope analysis. Isotope measurements can also be important in proving biogenic origin of an investigated sample. For the latter application, studies on C and S isotopes are particularly important because isotope fractionations of these elements are relatively well understood and their variations can be sufficiently large to be measured accurately. Among other biological relevant elements/isotopes, several metallic elements, such as Mn or Ni, are particularly attractive because of their roles in biocatalytic processes. Ni fractionation due to biological processes is expected, and there are several studies

showing fractionation could be about a few per mill.²¹ The isotope variations of these elements are typically very small, and as a result, their measurements were conducted, so far, exclusively using state-of-the-art laboratory sized techniques, such as SIMS, ICP-MS, or more specialized instruments.²² In the following, we present isotope measurements with emphasis on Ni using our miniature LIMS system^{4,21} designed for in situ studies of microscopic features in heterogeneous samples.

In this study, we apply our miniature LIMS system for accurate isotope analysis. The system was originally developed for in situ application in space research¹⁹ and consists of a reflectron-type time-of-flight mass analyzer coupled to an IR femtosecond laser system. The laser radiation is focused to a spot of 12 μm on the sample surface to ablate, atomize, and ionize the sample material. All formed cations are accelerated into the mass analyzer that allows separation and detection of them. The laser ablation ion source is enhanced by a double pulse (DP) laser unit, which allows an increase of the atomic ion concentrations and reduces abundances of clusters and molecular ions in the produced plasma plume.¹⁴ The studies are based on the depth profile measurement procedure, a technique developed in our group for the application in material sciences.²³ Depth profiling methods are common, and several analytical methods demonstrate their utility in analyses of the element distribution at surfaces and interfaces. The field of application ranges from the semiconductor industry, which, among other things, is interested to identify possible impurities within high purity functional materials of high performance,^{24,25} to geochemical and geochronology analysis in space and planetology research.^{26,27} By applying the depth profiling technique, the chemical composition of micrometer-sized inclusions can be well-isolated from the host elements, without extensive sample preparation.^{28,29} For larger samples, depth profiling offers also a means to gain information on sample homogeneity. But more importantly, because of the increased available statistics due to the profiling procedure, a filtering method can be applied which rejects, for example, mass spectra showing a poor spectral quality, spectra affected by significant isobaric interferences, or saturation problems of the detector system. This cleaning procedure, which will be discussed in the following in more detail, allows to quantify isotope ratios of, for example, small grained objects within a host material at the permille level.

2 | EXPERIMENTAL

2.1 | Sample material

For the validation of the analysis method, three samples were investigated, namely, (i) NIST SRM 968 Ni isotope standard, (ii) trevorite mineral localized within spinel mineral group, and (iii) micrometer-sized filamentous inclusions embedded in an aragonite mineral host. The sample material containing the micrometer inclusions was selected for these studies as it represents a natural, realistic case of geological material containing Ni, where spatially resolved chemical analysis is

required and sample preparation is limited. All samples were placed on a stainless steel sample holder and introduced into the vacuum chamber (Figure 1A).

2.1.1 | NIST SRM 968 Ni isotope standard

The NIST SRM 968 Ni isotope standard is a powder sample. We produced a circularly shaped pellet about 1 mm thick and in 5 mm in diameter by applying a pressure of a few MP for several minutes. The obtained pellet was subsequently placed in a dedicated cavity in the sample holder (see Figure 1A).

2.1.2 | Trevorite sample

The sample containing the trevorite mineral within Cr-Spinel grains was prepared as 30- μm -thick thin-section.³⁰ The sample originates from the mantle rocks of a Jurassic ophiolite in northern Greece.³¹ Trevorite is a rare nickel iron oxide mineral (described by NiFe_2O_4 as repeating unit). The mineral belongs to the Spinel group of the general formula: AB_2X_4 . The charges for A and B are 2^+ and 3^+ , respectively.

2.1.3 | Micrometer-sized inclusions embedded in an aragonite phase

Dark inclusions of micrometer dimensions are embedded in an aragonite phase hosted in serpentinized harzburgite. The sample was acquired from the slow-spreading Mid-Atlantic Ridge during ODP Leg 209 and collected from a depth of about 27 m below the seafloor.³² It was cut to prepare a 30- μm -thick thin-section (see also Tulej et al²⁸). The right panel in Figure 1 shows a close-up image of a sample area containing such dark micrometer inclusions at various locations and depths. Detailed information of these dark inclusions can be found in an accompanying paper.³⁰

2.2 | Laser ablation ionization mass spectrometer

The mass spectrometric studies presented in this contribution are conducted by our miniature reflectron-type time-of-flight mass analyzer coupled to an IR femtosecond laser ablation system. Details on the construction and operation of the instrument can be found in previous.^{3,4,19,33} The current study was performed in the vacuum chamber which was kept at a base pressure of mid 10^{-8} mbar. To avoid any vibrations from the turbo-molecular pumping system, including its roughing-pump (scroll pump), this pressure is sustained exclusively by an ion getter pump during measurements. The pulsed laser used for ablation was an IR (775 nm) femtosecond (~ 190 fs) laser operating at 1 kHz pulse repetition rate. The femtosecond laser beam has a Gaussian shaped cross section.

For the studies conducted on the trevorite mineral and dark inclusions in the aragonite, we employed the DP method to enhance the



FIGURE 1 (A) Samples are placed on a stainless-steel holder, in cavities, and stabilized by a cooper tape for UHV applications. (B) Sample material that contains the trevorite mineral (black area). White patches contain mostly the mineral spinel. (C) Aragonite host material (bright material) containing micrometer-sized inclusions (in black)

efficiency of the ion production and to reduce the abundances of cluster and molecular ions in the analyzed plasma plume. The DP method is described in detail in a recent publication.¹⁴ The DP unit splits the femtosecond laser beam into two beams, using a 50% beam splitter. One of these laser beams is delayed against the other, by passing it through a movable retro-reflector positioned on a 300-mm-long remote-controlled linear delay stage. The two beams are combined finally again using another beam splitter, resulting in a train of two laser pulses. A delay of about 40 ps is set between the two laser beams showing best performance by means of ionization efficiency and reduction of clusters and molecular species. Polarization-sensitive attenuators are used to adjust the pulse energy of each laser beam guiding system. The first laser pulse causes ablation and some ionization of the sample material, whereas the second (delayed) laser pulse is optimized for post-ionization and efficient fragmentation of clusters and molecular compounds in the ablated plume. Each beam can be blocked for conventional, single pulse (SP) laser ablation studies. A dedicated optical system guides the laser pulses towards the chamber, through an entrance window, through the mass analyzer, along its central axis, and finally down to the sample surface. The sample is positioned directly below the entrance of the ion optical system of the mass analyzer. The sample surface is remotely manipulated by an x, y, z-translation stage with micrometer positioning accuracy to be at the focal plane of the laser beam. Only positively charged ions are selected for the analysis in these studies. The ion detector consists of two microchannel plates (MCP's) arranged in chevron configuration and four centrosymmetric anodic rings.³³ The ion optical system is set in such way that most of the ions are directed towards one of the four anodes.³ The signal is recorded by a high-speed ADC card sampling at a rate of 2 GS/s and a dynamic range of 8 bit.

The sample surface was inspected by an in situ microscope-camera system prior to measurements to identify the measurement spots and to ensure overlapping of the laser spot with the defined areas of interest on the sample.³⁴ The overlap of the laser spot (diameter of $\sim 12 \mu\text{m}$) with the features on the sample surface can be made with approximately $2 \mu\text{m}$ accuracy.

2.3 | Mass spectrometric measurements

2.3.1 | Method

Mass spectra were collected at the locations identified from the images of the microscope-camera system allowing in situ imaging.³⁴ The number of laser shots was chosen by estimating first how fast the measured signals decay with depth. In case of the sample containing micrometer inclusions, a larger number of laser shots were applied to assure that there would be a sufficient number of ablated layers to reach the location of the inclusions within the host material. In the measurements conducted on the NIST and trevorite samples, typically 500 spectra were acquired, each of which being an accumulation of 100 single mass spectra. The 500 recorded mass spectra represent 500 layers ablated from the sample. During the measurements on the aragonite host, typically 300 mass spectra were acquired, each being an accumulation of 200 single mass spectra to increase the signal to noise (S/N) in the spectra. Mass calibration of the spectra, mass peak integration, and the spectra filtering procedure were discussed in details in our previous publications.^{23,35-37}

2.3.2 | Depth profiling analysis

The mass peaks of the relevant isotopes were integrated for each ablation layer and the obtained intensities, which are proportional to the number of recorded ions, were plotted as a function of ablated layer number. For homogenous samples, such as the currently used NIST SRM 986 Ni isotope standard, we observe a roughly exponentially decaying signal with depth. When using such laser radiation, the ablation craters are observed to be cone-like shaped and the depth of the crater is expected to be a few tens of micrometers.³⁸ For heterogeneous samples, the signal decay can be more complex as it will depend on the local physical and chemical properties of the sample along the ablated depth. Hence, the signal variations along depth can be used to isolate local inhomogeneity providing that applied laser

power densities are sufficiently stable in the course of the specific measurement campaign. Our laboratory studies indicate that with a depth resolution in the sub-micrometer range, regions of interests, such as individual mineralogical grains or mineralogical layers, can be detected relatively easily within the sample illustrating the high sensitivity of our miniature LIMS system.^{28,29,34,35,39}

2.3.3 | Data filtering

Using laser ablation, surface charging, space charge in the plume, and plasma variability are unavoidable. These effects can lead to intensity variations of mass peaks independent on the variation of the local elemental abundances, which is mitigated by the accumulation of spectra discussed above. In extreme cases, there is peak broadening and peak distortion, which in turn can lead to a significant decrease of the spectral quality (lower mass resolution and reduced peak intensities), which may affect the quantitative analysis by the mass peak integration. The presence of effects decreasing the spectral quality, such as mass peak broadening, shape distortion, or detector saturation reducing the peak intensity, influence measured mass peak intensities and can affect the derived isotope ratios. Recently, we developed a spectrum filtering software that allows for the identification and removal of the distorted mass spectra following a well-defined procedure.³⁷ Using a score function that describes the spectral quality based on selected mass peaks, spectra of bad quality are identified and removed from the analysis. The remaining mass spectra are subsequently used for further analysis.

2.3.4 | Mass peak intensity correlation

The intensities of the isotope peaks are obtained by the integration of the relevant peak areas in the mass spectra. When the peak intensity of one isotope is plotted as function of another isotope of that element, a linear correlation is observed. The slope determined from a linear regression yields the isotope ratio of the correlated isotopes. However, the determined isotope ratio may have contributions from isobaric interferences (from isotopes of other elements, clusters, and oxides having the same nominal mass). These effects can cause deviations from the linear correlation in addition to regular signal fluctuations due to variable laser ablation yields. Some of these effects can be identified and eliminated in the experiment. Isobaric contaminations will change the slope of the linear correlation or even make it deviate from a linear relationship. We find that data affected by isobaric interferences scatter more around the correlation line than the scatter of the isotope of the same element. This scatter is even more pronounced for isobaric contributions by clusters and molecular compounds. A systematic bending of the correlation curve is identified in the case of detector saturation.

By removing these data points, that is, the corresponding mass spectra, one can isolate the adverse contributions from the isotope ratio analysis. Moreover, we improve the precision of the isotope ratio

by restricting the analysis to the mass spectra which contribute data points within 2σ standard deviation obtained by linear regression fitting to the correlation line, effectively eliminating the isobaric contributions by clusters and molecular compounds. This intensity correlation method for accurate isotope ratio analysis, presented in the following in more detail, can be compared with the isochrone analysis of minerals for their accurate age determination. In comparison to the age derived from a single measurement conducted on a single mineral the slope of the isochrone derived from various measurements conducted on different minerals provides a much more accurate age because fluctuations induced by, for example, measurement instabilities are smoothed out by this procedure.⁴⁰

2.3.5 | Spectra analysis and isotope ratio calculation

Analysis of peak shape and mass resolution, spectrum calibration, and peak integration are fully automatized and performed by a custom software package written in Matlab.^{36,37} The isotope abundances are calculated from the integration of the relevant isotope mass peaks and given in the δ -notation:

$$\delta^n X = \left(\frac{{}^n X_{\text{exp}} / m X_{\text{exp}}}{{}^n X_{\text{std}} / m X_{\text{std}}} - 1 \right) * 1000,$$

where X represents a certain element, whereas n and m represent two isotope numbers, and $\delta^n X$ is given in permille. *Exp* and *std* stand for experimentally determined and standard isotope abundance values, respectively. The latter are taken either from NIST SRM 986 spec sheet for the Ni isotopes or as stated for the natural abundances of the isotopes.

3 | RESULTS

3.1 | NIST SRM 968 Ni isotope standard

A raw mass spectrum consisting of the five Ni isotope mass peaks measured on the NIST SRM 968 sample is shown in Figure 2A (black line). All 500 spectra recorded for 500 ablation layers are accumulated to obtain this raw spectrum. The individual peak intensities plotted as a function of ablation layer are depicted in Figure 2B, where a slow signal decay with a depth is observed. Although peak intensities fluctuate from spectrum to spectrum, the fluctuations of the isotope peaks are observed to correlate well. The Ni spectrum is measured with around four decades of dynamic range at a mass resolution of about $m/\Delta m \approx 250$. The S/N is sufficiently high to reach an isotope accuracy at the per mill level for the raw data.⁴¹

With the support of the spectra filtering method discussed above, the spectra containing distorted or broadened mass peaks were identified and excluded from accumulation during data analysis,³⁷ improving spectral resolution and peak shape (spectrum in red, Figure 2A). As can be clearly observed, the tails of the mass peaks do not overlap

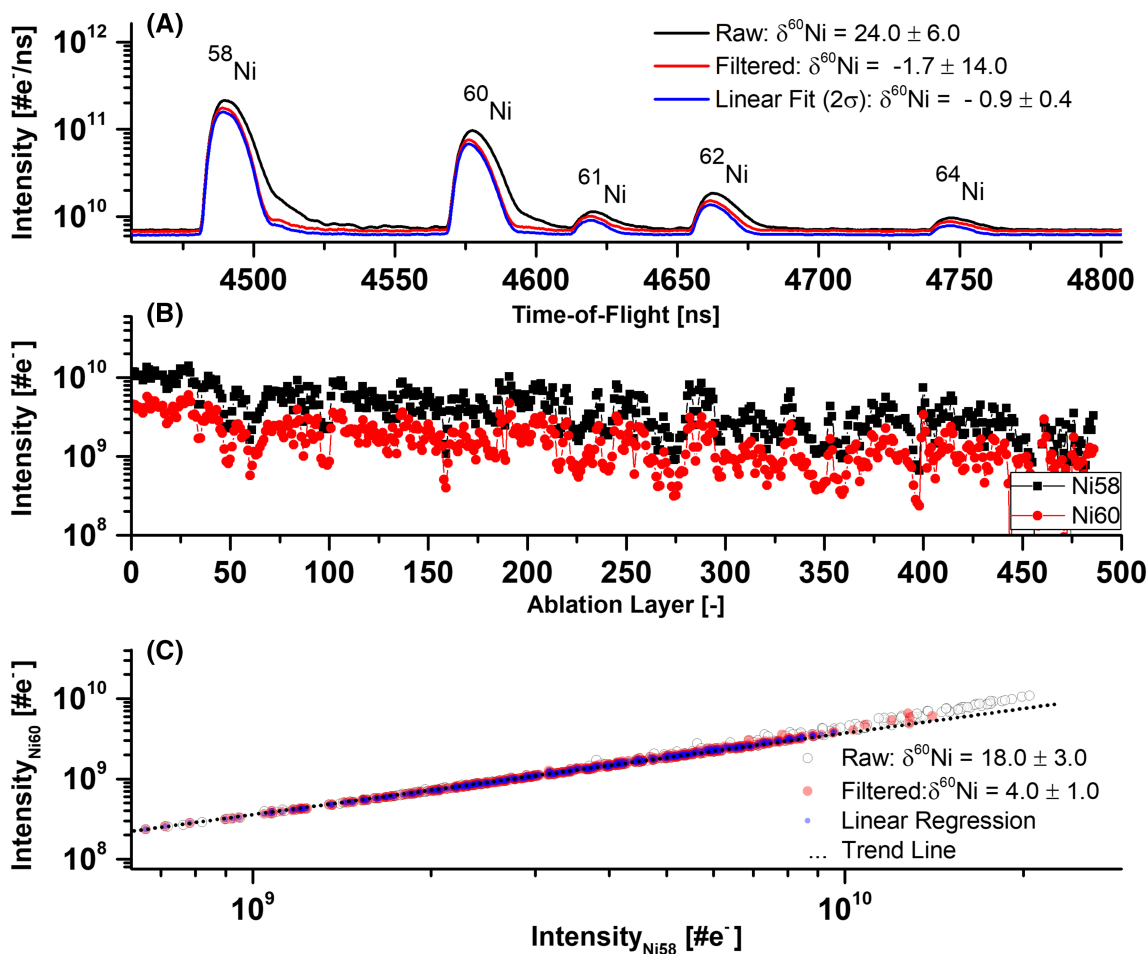


FIGURE 2 Panel (A) shows the Ni isotope TOF spectra: A raw spectrum (black line) is obtained after accumulating 500 spectra recorded from one sample location; the spectrum shown in red results from removing the distorted spectra from the raw spectra and the spectrum shown in blue is finally obtained after removing the spectra corresponding to the data by the 2σ selection (see panel C). Panel (B) shows the individual data for the depth profiles of the ^{58}Ni and ^{60}Ni isotope mass peak intensities derived for each of 500 ablation layers. Panel (C) depicts the ^{60}Ni concentrations as function of the ^{58}Ni concentrations for raw data (open circles), after spectral filtering (red filled circles), and after removing data points deviating by 2σ from the fit to the red data points (blue filled circles)

anymore with each other and the shape of the mass peak is Gaussian compared to the raw mass peak shape (in black). The score function used by the filtering method is plotted in Figure 3, using the ratio of the mass resolution to peak fit area error (details in Wiesendanger et al.³⁷). After investigating the isotope ratio and S/N as the function of the score value, we derived a score value 1,300 as threshold for good quality mass spectra; spectra with a lower score value are discarded. For this spectrum cleaning, we get the maximal S/N and an isotope ratio of $\delta^{60}\text{Ni} = 4 \pm 1$ from the slope in Figure 2C, which is close to the value of the NIST 968 standard (Figure 3B). Nevertheless, the procedure reduces the number of spectra available for the calculations of the isotope ratio, typically, with about 70%–90% spectra remain after using the filtering procedure. Using larger score values, the mass resolution improves, but the precision of the isotope ratio becomes worse because the S/N becomes smaller.

A linear correlation is observed only for the intensities of the ^{58}Ni mass peak for signals lower than $5 \times 10^9 \#e^-$. For larger intensities, the correlation curve derived from the raw data (open circles) deviates

from the linearity (see trend line and the correlation curve in Figure 2C). The ^{58}Ni isotope mass peak intensities become underestimated due to a decrease of the detection efficiency of the MCP detector system (detector saturation) at these high ion intensities. The red-filled circles remaining after application of the spectrum cleaning procedure do not remove all the data points measured with detector saturation. By applying the linear regression to the red points, one can further identify data points that are outside the trend line. In addition, we apply the 2σ selection for the mass spectra for the final accumulation and calculation of the isotope abundances by the mass peak integration, where σ is the standard deviation obtained from the linear regression fit to the linear part of the correlation curve. Mass peak integration is the merging of all filtered/fitted data into a single composite spectrum from which the isotope ratios can be determined by integrating peak pairs. The distribution of the data points from the fitted trend line is plotted in Figure 2C.

The slope obtained by the linear correlation yields the ratio between the ^{60}Ni and ^{58}Ni isotopes of $\delta^{60}\text{Ni} = 4 \pm 1$ after the spectra

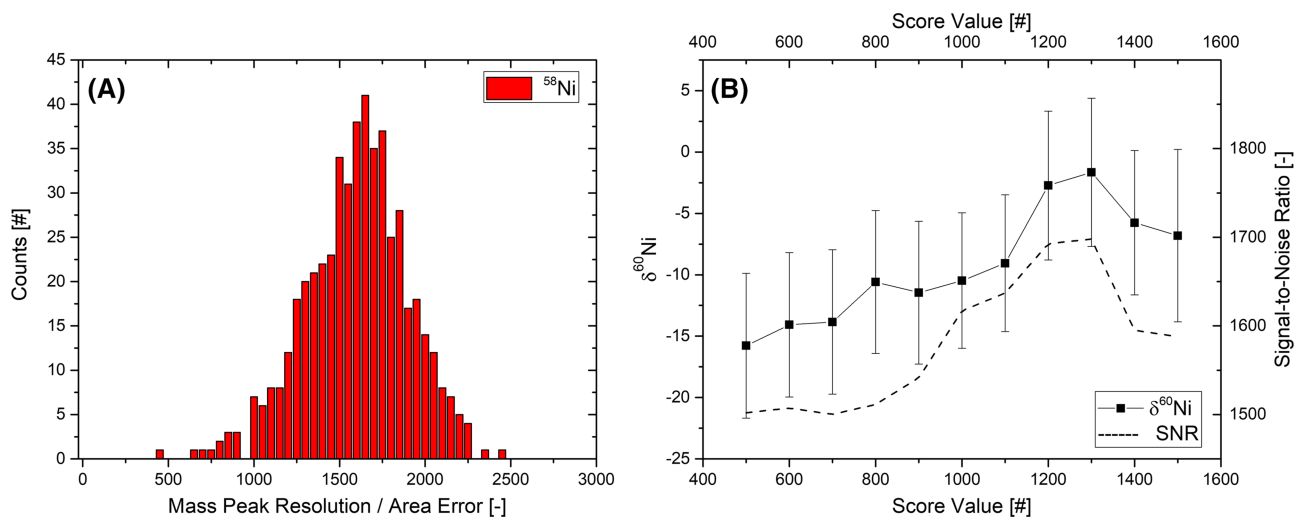


FIGURE 3 Analysis of the Ni isotope ratios for the NIST SRM 968 sample: Panel (A) the score function derived from the ratio between the mass peak resolution and area error. Panel (B) shows the ^{60}Ni isotope ratio in permille, and the signal-to-noise ratio as function of the score value

filtering. The $\delta^{60}\text{Ni}$ values obtained by the linear fit are typically very close to that obtained by the integration method and both values are significantly more accurate than the ratios determined from the raw data: raw data $\delta^{60}\text{Ni} = 24 \pm 6$, filtered $\delta^{60}\text{Ni} = -1.7 \pm 1.4$, and the final result after 2σ selection is $\delta^{60}\text{Ni} = -0.9 \pm 0.4$. The mass spectrum obtained by summing the spectra remaining after filtering and constraining by the linear regression methods is shown in Figure 2A (in blue). This spectrum is used finally to derive the isotope concentrations by the mass peak integration, which resulted in $\delta^{60}\text{Ni} = -0.9 \pm 0.4$. The presented procedure yields a determination of the $\delta^{60}\text{Ni}$ value in very good agreement to the values given for NIST SRM 968 and is in the following applied for the analysis of other more complex samples.

The individual results obtained from the analysis of 10 locations are shown in Figure 4. The individual measurement accuracies are typically within a few per mill. These values have also comparable errors to that of δ values. To increase the accuracy and precision of the measurements, an increased number of measurements will be necessary. Taken these 10 measurements together, we obtain a mean value of $\delta^{60}\text{Ni} = 0.47 \pm 0.68$. Although the results obtained in these studies do not reach accuracy and precision of the other well-known laboratory techniques (multicollector MS, SIMS), nevertheless, we demonstrate that isotope ratios of some stable isotopes can be measured at the single per mill level, which is very useful for in situ investigations in planetary science.

3.2 | Trevorite

A typical mass spectrum of the trevorite mineral sample obtained by accumulating 600 spectra on one sample surface location is shown in Figure 5A. The spectrum was measured with more than four decades of dynamic range. The mass resolution of the main peaks ranges from $m/\Delta m \approx 230\text{--}350$. From our mass spectra, the presence of the

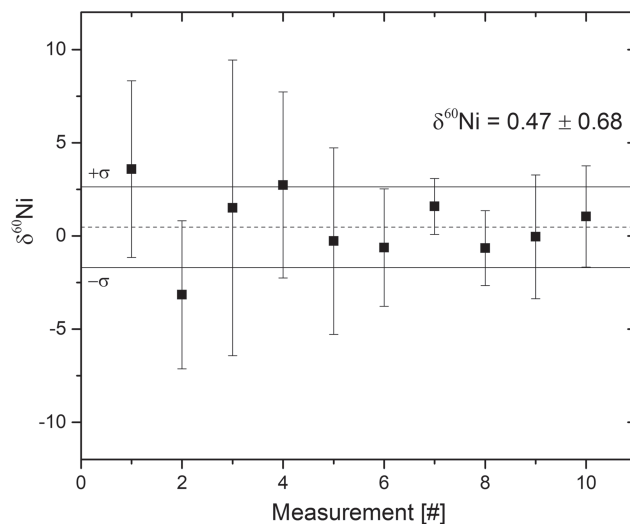


FIGURE 4 The summary of the Ni isotope analysis. The data are obtained from measurements on 10 locations on the NIST SRM 968 Ni isotope standard

trevorite mineral, based on the relevant elements and their abundances, can be clearly observed. Several major elements are measured at the sample location including the Na, Mg, K, Si, Cr, Fe, and Ni, in agreement with the expectations for the trevorite mineral.³¹ Additionally, minor species, such as B, Al, Mn, Co, Ca, and Cl, are identified as well. The relative sensitivity coefficients (RSC) of metallic elements are typically close to one whereas the sensitivity for O is less than one and has to be corrected with the RSC factor which effectively increases the abundance by about two to three times, depending on the ablation conditions and the physicochemical properties of the investigated material.⁴²

The concentration ratio of the Fe/Ni obtained by integration and subsequent normalization to the element concentrations is close to 2, whereas the ratio for O to Ni concentrations is about 1.9. The

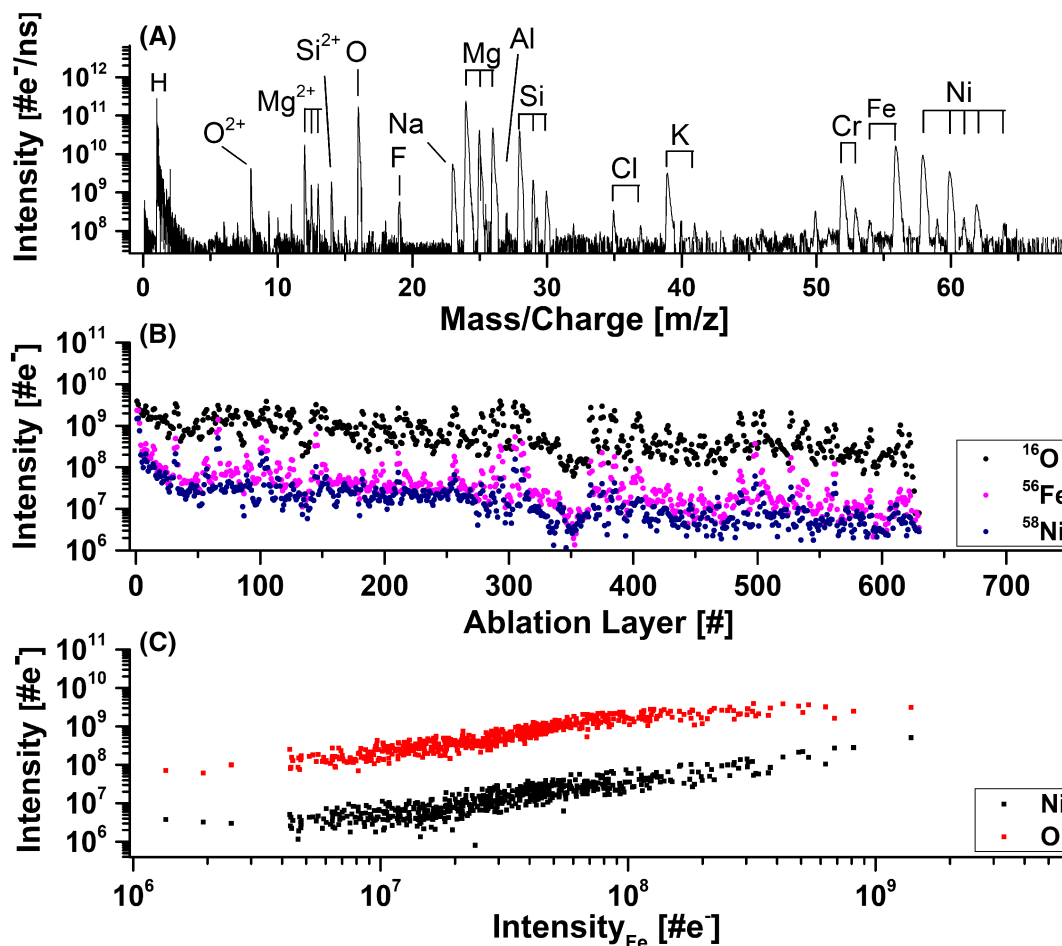


FIGURE 5 Panel (A) shows the mass spectrum of the trevorite mineral (spinel group). Panel (B) shows the element concentration variation with depth, and panel (C) depicts the concentrations of the elements Ni and O as function of the Fe concentration

depth profiles of the Fe, O, and Ni elements are shown in Figure 5B. Again, and as expected, the measured mass peak intensities are observed to decrease with the depth. The intensity ratios of O, Ni, and Fe correlate along the depth indicating relatively high degree of homogeneity of the sample at this location over the sampled depth range. Also, the intensity correlation curves (Figure 5C) show a fairly linear dependence, aside from the saturation of the O signal at high intensities, and with some scatter due to the signal fluctuations.

Figure 6A,B shows the spectra of the elements Mg and Ni obtained by summing up all the spectra selected remained after the spectra filtering and linear regression selection. In the latter spectrum, also the peak of the ⁵⁶Fe isotope is shown for comparison. The Fe intensity is sufficiently high that the isobaric interference due to presence of ⁵⁸Fe over determines the ⁵⁸Ni abundance and the $\delta^{60}\text{Ni}$ value becomes larger by about -1 to 3 per mill, which is accounted for in the analysis. The depth profiles of the mass peak intensities of the Mg and Ni isotopes are plotted in Figure 6C,D, respectively. The quality of the mass peak intensity correlation can be observed in more detail from the plots in Figure 6E,F for Mg and Ni isotopes, respectively. The open circles represent data points derived from the raw mass spectra while the red-filled circles are the data points after elimination by the data filtering method. Similar to the NIST standard, the linear

correlations between the Mg (Figure 6E) and Ni (Figure 6F) isotopes improve the selection of data points for the isotope analysis. In the high peak intensity range, the ²⁴Mg isotope signals are observed to be underestimated, followed by increased scattering of the data. The correlation becomes more confined after spectra filtering. In contrast, the correlation of the Ni isotopes is close to linear for higher intensities, but data scatter more at lower mass peak intensities, caused by signal fluctuations. The filtering method allows to remove several data points in the scattered part of the correlation curves. For this data analysis, the score value of 600 is applied (see also Wiesendanger et al³⁷). The isotope abundances for this location derived after the spectral filtering and by 2σ selection are $\delta^{26}\text{Mg} = -0.9 \pm 1.0$ and $\delta^{60}\text{Ni} = -0.9 \pm 1.6$, which are in reasonable agreement with the expected values from their standard isotope abundances of both elements.⁴³

The data points for several locations on the sample scatter considerably more than in the case of the measurements on the NIST isotope standard, indicating that peak fluctuations are larger in the rocky sample compared to the measurement on the metallic NIST sample. Flattening of the Ni isotope correlation curve for the highest intensities indicates that the ⁵⁸Ni mass peak intensity may increase relative to the ⁶⁰Ni mass peak intensity. This can only be possible when at

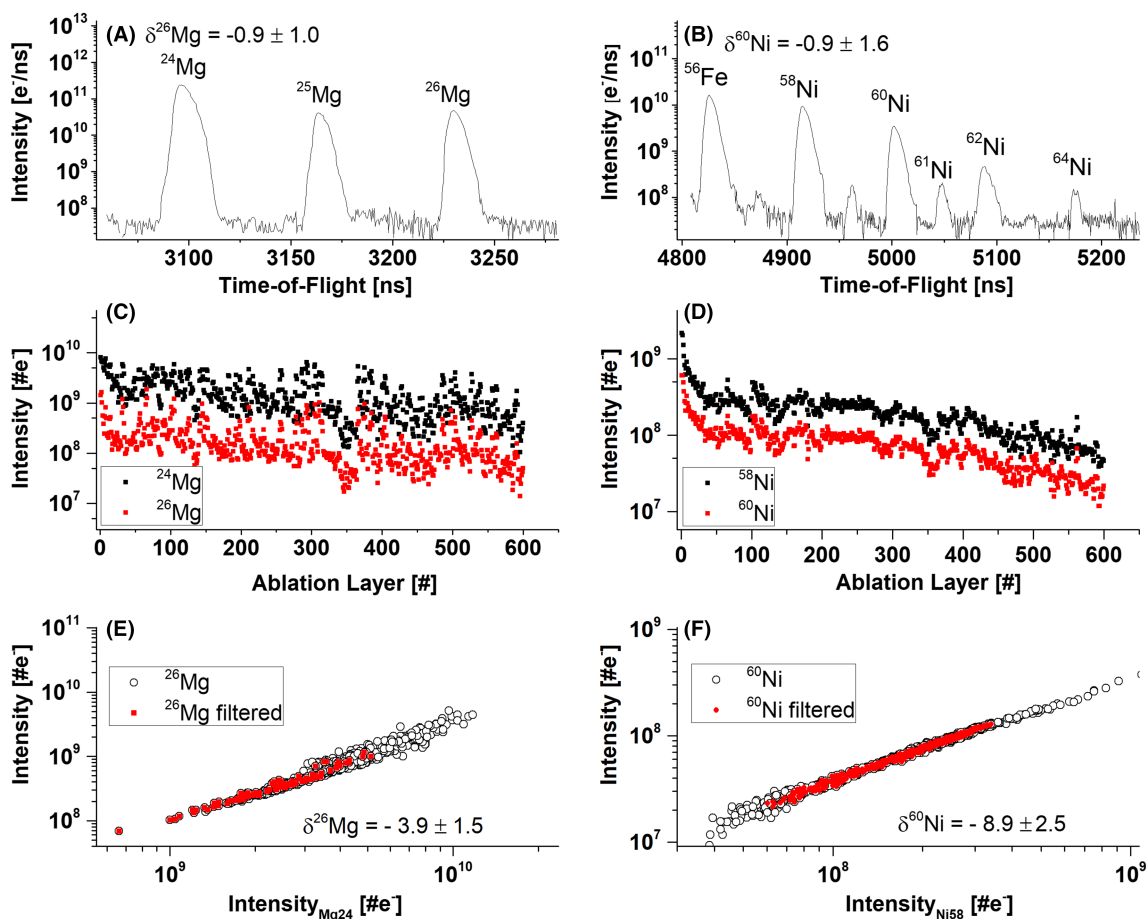


FIGURE 6 Panels (A) and (B) show the Mg and Ni isotope spectra from the trevorite mineral, respectively, after applying the spectra cleaning procedure. In panel (B), the mass peak of ^{56}Fe isotope is also shown. Panels (C) and (D) show the depth profiles for the Mg and Ni isotope mass peak intensities (raw data), respectively. Panels (E) and (F) show the isotope mass peak intensity correlations for the Mg and Ni isotopes, respectively

these high intensities the isobaric mass peak intensities due to ^{58}Fe and $^{26}\text{MgO}_2$ could increase nonproportionally and contribute to the signal of the ^{58}Ni isotope. Another possibility is that the spectral quality (peak shape distortions) limits the mass peak integration accuracies. Because the data points in this part of the intensity correlation curve were discarded by the filtering, the latter effects are more likely to contribute. In spite of removing of about 400 and 200 spectra in the calculations of the isotope ratios of Mg and Ni, respectively, the accuracy and precision at the few per mill level can be achieved for the analysis from the individual sample locations.

The results summarizing the Mg and Ni isotope studies on 10 sample locations are shown in Figure 7A,B, respectively. Again, the accuracies and precision of the Mg and Ni isotopes can be determined at the single per mill level. The $\delta^{60}\text{Ni}$ values are corrected by the contribution from the underlying isobaric ^{58}Fe mass peak intensities. These are derived from the measured ^{56}Fe mass peak intensity and the quoted standard abundance value for the ^{58}Fe isotope. Taking the 10 measurements together we obtain $\delta^{26}\text{Mg} = -0.13 \pm 0.96$ and $\delta^{60}\text{Ni} = -0.30 \pm 1.15$. Similar to the NIST studies, more accurate isotope ratio values are expected to be obtained for larger number of measurements.

3.3 | Micrometer inclusions embedded in an aragonite crystal phase

In Figure 8A, a typical mass spectrum recorded from a dark inclusion (see Figure 1A) embedded in the aragonite host is shown. The spectrum was measured with four decades of dynamic range and a mass resolution of $m/\Delta m \approx 300$ for the different Ni peaks. In mass spectra of such micrometer inclusions, we identified biologically relevant elements (C, H, N, O, P, and S), a number of metallic elements including V, Cr, Mn, Fe, Co, Cu, Se, and Ni, which are known to be bio-essential.⁴⁴ Traces of the B, F, and Cl are identified, which are elements likely contributed from seawater. Trace amounts of the elements Ti, As, and Sr are observed as well: Ti is a very common element on Earth,⁴⁵ Sr is known to be present in carbonates,⁴⁶ and As has been associated with hydrothermal activity and weathering.⁴⁷ These elements are identified within first 10–140 ablation layers at the uppermost sample subsurface but were not found in the aragonite host phase (Figure 8B,C). The first 10 ablation layers were discarded because of large signal fluctuations due to the initial formation of the ablation crater. The element intensity correlations show a fairly homogeneous material along the ablation depth. The higher peak intensities

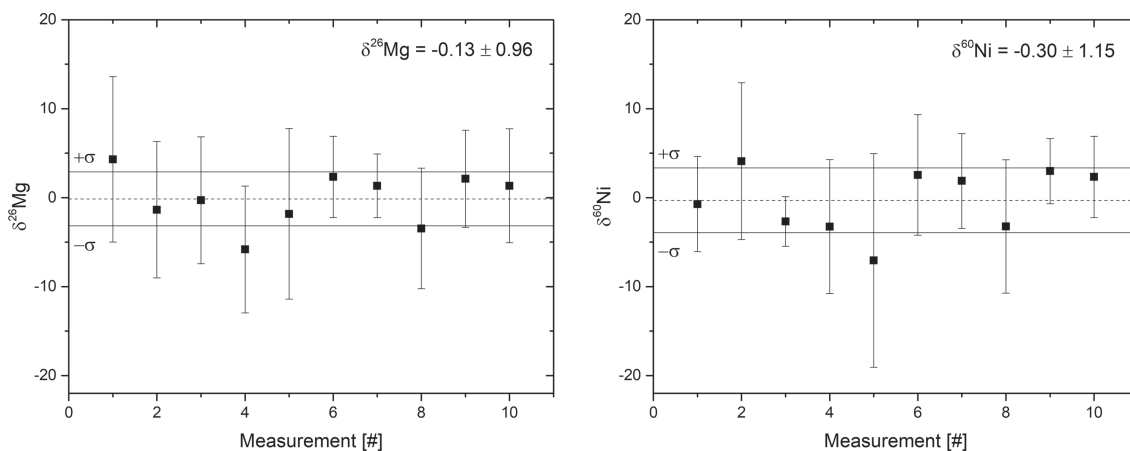


FIGURE 7 The summary of the isotope analysis conducted on 10 sample locations on the trevorite mineral

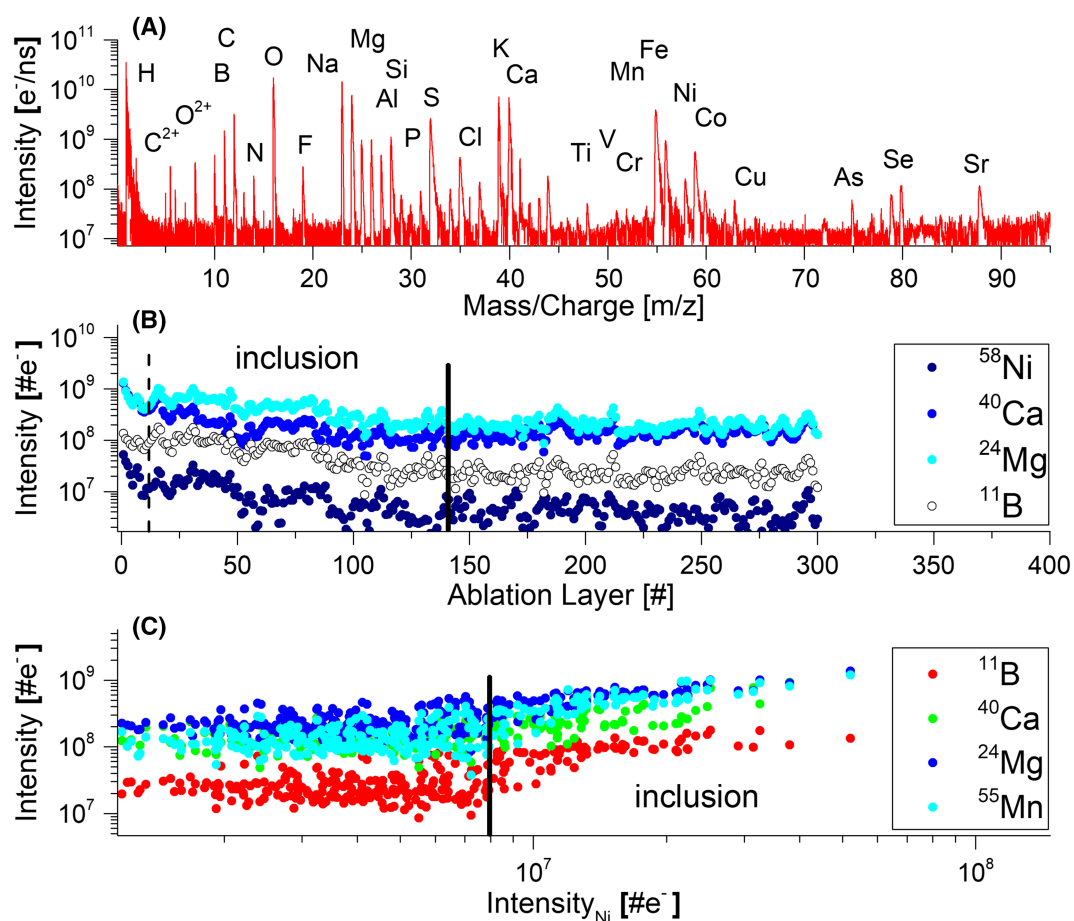


FIGURE 8 Panel (A) shows the mass spectrum recorded at the location of a micrometer inclusion in the aragonite sample. Panel (B) shows the depth profiles for the mass peaks of isotopes several elements. Panel (C) shows the B, Ca, Mg, and Mn intensities as function of the Ni intensity. The black vertical line indicates where the signal becomes too small to be used for accurate analysis

for all the elements including C, O, and Ca (carbonate phase) for the first 140 ablation layers is because of the improved ablation efficiency of the dark structures due to enhanced absorption of the laser radiation at this location. The signals of elements other than C, O, Mg, and Ca are observed to fade at depths beyond 140 ablation layers. Thus, for the elements Ni and B, the analysis was limited to the layers 10 to

140, whereas for the Mg isotope analysis, all ablation layers were used. Almost linear correlation between the Ni and other elements is observed for the intensities larger than $8 \times 10^6 \text{ #e}^-$ (Figure 8c).

The spectral analysis is following the same method developed for analyzing the NIST isotope standard. For this sample, here, isotope ratios are analyzed for the elements B, Mg, and Ni. In Figure 9A–C,

the depth profiles of the element isotopes are shown. Although the depth profile of the Mg isotopes extends to the entire depth range of 300 ablation layers, a plateau after around 100 ablated layers can be observed for the other elements B and Ni. Therefore, only the layers 10–140 are considered for the B and Ni isotope analysis whereas the signals of all ablated layers are considered for Mg isotopes. In Figure 9D–F, the intensity correlations of the B, Mg, and Si isotopes are displayed. Again, all data points are represented as open circles and data selected by spectral filtering and 2σ selection by red full circles. The score function of 500 is applied here hence slightly lower than in the case of the trevorite data analysis. Although the data points are observed to be well-constrained to the trend line for the Mg isotope correlation, the data points of the B and Ni isotopes measurements scatter more around the correlation curves. This observation can be attributed to signal fluctuations here rather than other effects. In Figure 9G–I, the mass spectra of the B, Mg, and Ni isotopes obtained by summing up selected mass spectra obtained after spectral filtering and 2σ selection are displayed. The spectra of the Ni isotopes are shown with the mass peaks corresponding to the neighboring elements Mn, Fe, Co, and Cu. The isobaric interference from the ^{58}Fe

peak is accounted for in the analysis, as well as the overlap from adjacent peaks for the determination of isotope ratios. In spite of the small number of spectra taken for the analysis, the $\delta^{60}\text{Ni}$ value is stable within a few per mill when applying spectral filtering and accepting all the spectra within 2σ deviation from the trend line obtained by the linear regression.

In total, four different locations containing such dark, micrometer-sized inclusions were investigated. Following the isotope ratio analysis discussed above for one surface position (Figure 9), we derived a mean value for $\delta^{60}\text{Ni}$ of -3.32 ± 0.81 . In total, eight measurements were used for the Ni isotope analysis; however, three out of the eight measurements were affected by isobaric interference with the mass peak of the C_5 cluster. For the affected measurements, a significantly higher $\delta^{60}\text{Ni}$ value in the range of about 15–20 was observed, which was the reason why these measurements were discarded for the calculation of the final value. For B, we derived a mean value of $\delta^{11}\text{B} = -46.1 \pm 2.9$ (based on eight measurements) that corresponds to a ratio of $^{11}\text{B}/^{10}\text{B} = 3.84 \pm 0.68$, which is significantly lower than the isotope ratio of terrestrial abundances (~ 4.03). Theoretically, the ^{10}B peak can be affected by the quadruply charged calcium

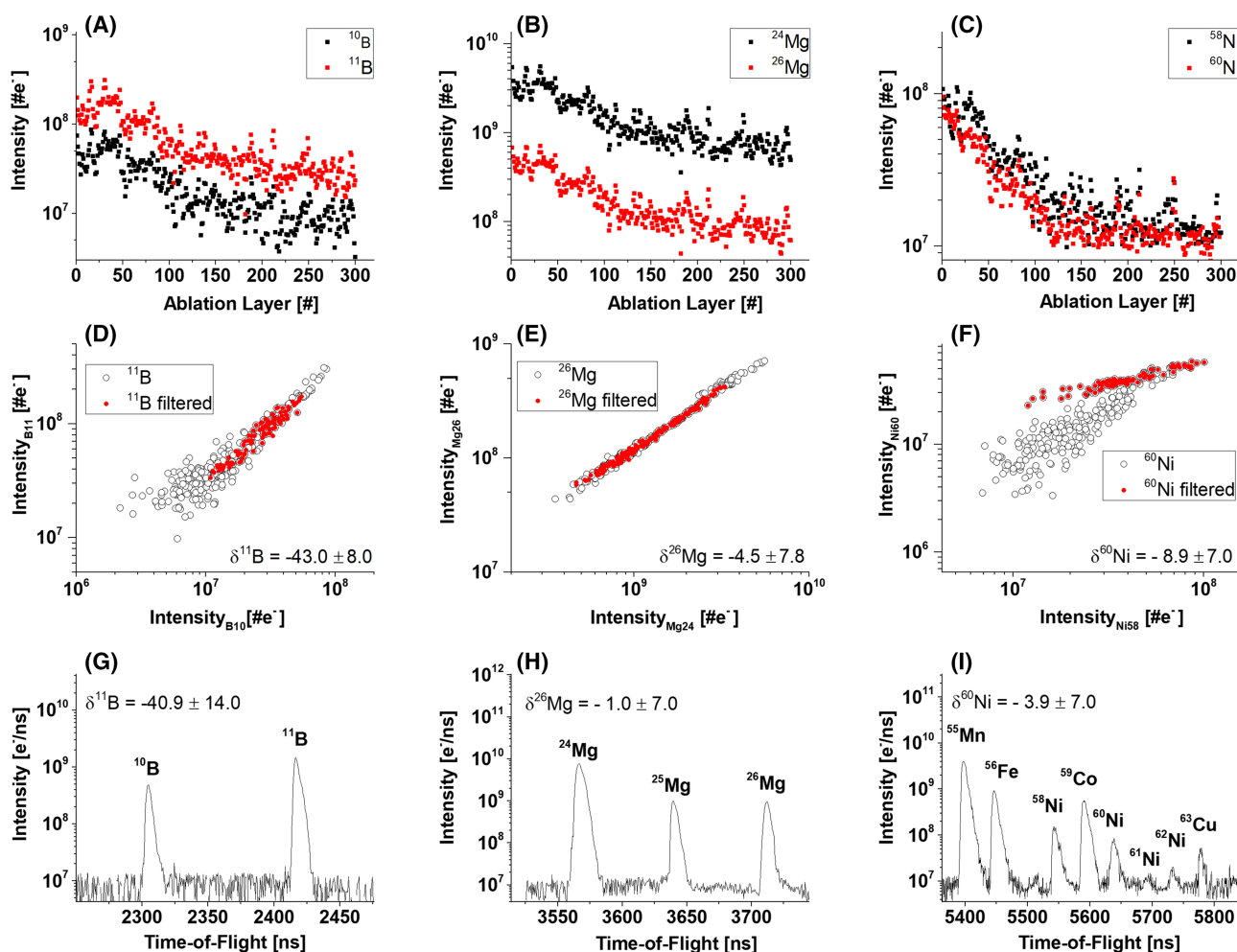


FIGURE 9 Panels (A–C) show depth profiles for the B, Mg, and Ni isotopes at the location of a dark, micrometer inclusion in the aragonite sample. Panels (D–F) show the isotope intensity correlations as raw data points (open circles) and after spectra filtering (full circles). Panels (G–I) show sections of the recorded time-offlight spectra of the elements B, Mg, and Ni with their isotopes

isotope ($^{40}\text{Ca}^{4+}$), but the relevant mass peaks of the doubly and triply charged ^{40}Ca are either too weak or not present. Thus, it is unlikely that an isobaric interference plays the role here. Therefore, the $\delta^{11}\text{B}$ results indicate that the observed isotope fractionation is a result of natural processes having occurred in the sample, likely because of isotope fractionation effects in the seawater depending on pH level.⁴⁸ For Mg no statistical value, similar to B and Ni, can be presented here. As discussed earlier, the measurements for this type of sample material were optimized for a high S/N of Ni, which resulted in most cases in a saturated Mg signal.

3.4 | The effects of clusters and molecular ions

Figure 10 compares the mass spectra recorded with the single pulse (SP) (in red) and double pulse (DP) (in black) laser ablation ionization method for the trevorite mineral and the dark, micrometer-sized inclusion in the aragonite phase, respectively. The mass resolution of the mass spectra ($m/\Delta m \sim 250\text{--}300$) is too low to resolve possible interferences due to clusters and molecular ions directly. In the mass spectrum of the trevorite mineral, the isotope abundance measurements of Mg are not affected by any isobaric interference, but the ^{58}Ni and ^{56}Fe isotope peaks can be affected by the presence of the MgO_2 and Si_2 isotopes; thus, the value of the abundance of ^{58}Ni would be overestimated if that is not accounted for. Si and Mg clusters and their oxides are produced during the laser ablation and can be identified in the SP spectrum (see Figure 10). Thus, with the SP method it will not

be possible to conduct an accurate isotope analysis for Ni. In the spectra recorded on micrometer inclusions, C_2 , C_2H , and C_2H_2 compounds formed during laser ablation can interfere with the Mg isotopes, and the Si_2 , MgO_2 , CaO , and C_5 compounds can interfere with the Ni peaks. This can be anticipated again from the observation of the family of the C, Mg, Si, and Ca compounds in the SP mass spectrum. Generally, the cluster families X_n^+ and oxide families X_nO_m (with X being C, Mg, Si, Ca, and $n = 1\text{--}3$, $m = 1\text{--}3$) are observed over the entire mass range of the spectrum. These compounds are frequently observed in the laser ablation studies at the applied laser power densities. The isotope components of Si_2 and MgO_2 will increase the intensities at mass 58, and if not corrected well, the ^{58}Ni mass peak is overestimated and will decrease the apparent value of $\delta^{60}\text{Ni}$. In case of the aragonite sample, the Ni isotope ratios can be affected also by the ^{42}CaO oxide and $^{12}\text{C}_5$ cluster causing the intensity contributions to the ^{58}Ni and ^{60}Ni isotope components, respectively.

The DP mass spectra show a significant improvement with respect to the dynamic range and reduction of these isobaric interferences. Nevertheless, experience shows that even when using the DP method, cluster and molecular ions cannot be completely removed from the plasma plume.¹⁴ An inspection of a few mass spectra measured on the trevorite mineral and the micrometer inclusions with the DP method show sometimes some weak mass peaks that can be assigned to clusters and oxides. Mg isotope abundances determined on dark inclusions can be affected as well by isobaric interferences due to possible presence of C_2 clusters and C_2H and C_2H_2 molecules. Such a presence would show as an increased abundance of the ^{24}Mg isotope and would

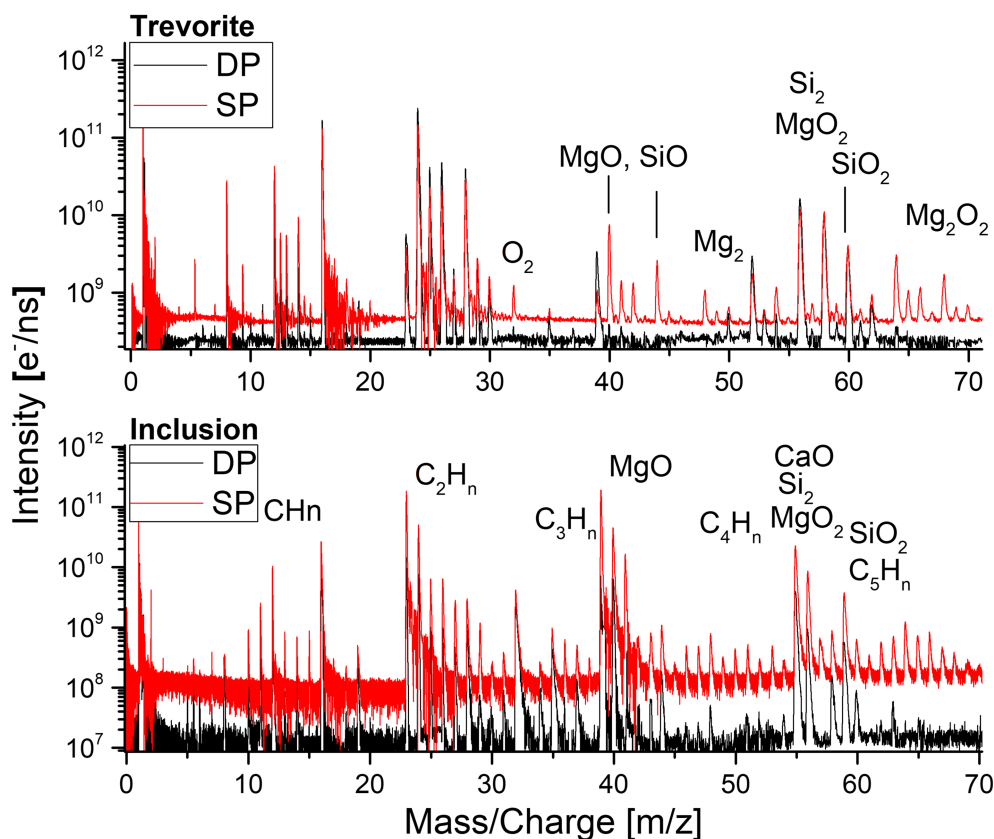


FIGURE 10 The single pulse (SP) and double pulse (DP) mass spectra of trevorite (upper panel) and dark inclusion in the aragonite phase (lower panel). Locations of clusters and molecular ions are indicated in the figure, as they can be identified in the SP mass spectra. The clusters and molecular ions are reduced when using the DP method

result in lowered $\delta^{26}\text{Mg}$ values. We estimate that the effect to possible influence of isobaric interferences on the Mg isotopes, if present, is relatively small, at the single per mill level at most.

In the mass spectrum of the trevorite mineral, peaks at mass 40 (MgO), 48 (Mg_2), 56 (MgO_2 , ^{56}Fe -present), and 64 (Mg_2O , ^{64}Ni -present) are not observed hence one can expect that the contribution of the MgO_2 oxide to the mass peaks of ^{56}Fe and ^{58}Ni is also absent or negligible.¹⁴ This can be concluded from the isotope analysis of the Fe isotopes considering also the corrections due to the presence of the ^{54}Cr isotope. These values were measured with accuracies at a few per mill level. Similarly, one can make estimates for the contribution of the Si compounds to the peak intensities from the absence of the masses 44 (SiO), 56 (Si_2 , ^{56}Fe -present), 60 (SiO_2 , ^{60}Ni), and 72 (Si_2O). We conclude that the only possible interference to the derived isotope ratios is expected from the isobaric interference due to the ^{58}Fe isotope. The concentrations of this isotope, as derived from the analysis of the ^{56}Fe mass peak, is sufficiently high to overestimate the concentration of the ^{58}Ni isotope by about one per mill. These corrections to the $\delta^{60}\text{Ni}$ values are included in the analysis. Similar conclusions are reached analyzing the dark inclusions embedded in the aragonite host.

4 | DISCUSSION

For accurate and precise isotope analysis using our LIMS system, high-quality mass spectra by means of mass resolution and dynamic range are of utmost importance. Due to the small size of the ion optical system of our LIMS system, space charge effects, sample surface charging, and detector saturation can have a significant impact on the spectra quality, and a robust analysis method for isotope analysis is required to reduce these effects to a minimum. Other unavoidable effects are the variability in the plasma plume formation, which are mitigated by the accumulation of mass spectra. However, the number of accumulated spectra is of high importance because the S/N level can be improved by this procedure, which in turn improves the dynamic range and therefore the measurement accuracy. In this study, the number of spectra remaining for the final analysis, after our filtering methods, is reduced from initially 60,000 single-shot spectra to 20,000–30,000. Thus, the losses pertaining to statistics are negligible. Moreover, we demonstrated that the spectral filtering and the 2 σ selection can identify many of the effects affecting the accuracy of the isotope analysis. The presented and successfully applied method improves significantly the accuracy of the isotope ratio analysis and allows the reproducibility of such measurements. Nevertheless, the method applied here removes significant number of mass spectra from the analysis and has to be applied with care. Moreover, the 2 σ selection artificially improves apparent measurement δ -value precision. Nevertheless, the precision the δ -value measurement is in this case limited more by the δ -value fluctuation within individual measurements. These values are typically within several per mills.

It is obvious that for the quantitative analysis, a sufficiently high S/N and good mass resolution are required.³⁶ Our instrument can be

operated for geological samples routinely at about five decades of dynamic range by accumulation of about 40,000–60,000 of single-shot mass spectra (see, e.g., Figures 2, 5, 8, and 9). In the analysis of the Ni isotopes on the NIST Ni isotope reference sample, the Ni peak intensities can be measured within the dynamic range of the instrument. However, the Ni peak intensities in the spectrum of trevorite were observed at least at 10 times lower intensity, and the Mg peak intensities were measured with a dynamic range of about 4.5 decades. Ni peaks in the spectra of the dark inclusions have comparable or lower intensities compared to that of the trevorite mineral.

In our earlier studies on the analysis of metallic samples, we have shown that for the signal intensities corresponding to abundances larger than 50–100 ppm (atomic fraction), our instrument can conduct isotope measurements with an isotope accuracy at the per mill level.^{3,41} Here, we achieved similar accuracies for B, Mg, and Ni for the three different samples.

Typically, the depth profiling measurement procedure allows the investigation of the chemical homogeneity of the sample in one spatial dimension. With a depth resolution at submicrometer level, small embedded objects or layering of minerals can be identified by the elemental correlation within the ablation layers of a distinct chemical composition. Such studies can be conducted providing that the atomic intensity variations are significant to identify them. Additionally, the depth profiling method allows to investigate ablation mechanisms, ablation rates, and crater structures.^{35,49} Based on the homogeneity of the trevorite sample, we found in the current study that the depth profiling method allows to investigate the influence of space charge, sample surface charging, plasma variability, and isobaric interferences by clusters and molecular compounds on the measurement quality. These effects can be inferred because of the high stability of the applied femtosecond laser radiation intensities and the good stability of the ion yield production. A high degree of this stability is reflected in the linear correlation of the isotope mass peak intensities providing that no other effects affect the isotope abundance ratio.

As stated earlier, mass spectra showing a poor mass resolution and distorted peaks are removed by the filtering method to a large extent. From the intensity correlations, detector saturation can be easily detected by the deviation from linearity of the isotope mass peak correlation curve starting at certain mass peak intensities (e.g., Figure 2C). The rejection of all data points except that correlating linearly ensures that both the spectra affected by detector saturation effects and the spectra with low intensity mass peaks are removed from the final analysis, which in turn results in the improvement of isotope ratio analysis. Together, this analysis procedure allows the determination of isotope ratios at the level of a few per mill. The detector saturation is observed in the analysis of the Mg isotope spectra measured on the trevorite mineral. The measurements conditions on the trevorite mineral were optimized initially to obtain largest possible signal intensities for the Ni isotopes. Hence, the Mg isotope measurements were suffering from detector saturations. The isotope mass peak intensities derived from only about 30% of all the recorded spectra show the linear dependence. For the correlation curve of the

Ni isotopes, the linearity is achieved in the middle range of the Ni isotope intensity range. Here the Ni data scatter more, which is likely due to Ni peak intensity fluctuations, but the increased scatter can also be introduced by contribution from isobaric interferences by ^{58}Fe and MgO_2 . The peak intensities for Fe and MgO_2 typically show larger fluctuations and are much less correlated with the Ni isotope peak intensities. The Ni isotope value we measured on the trevorite mineral of $\delta^{60}\text{Ni} = -0.30 \pm 0.16$ is still outside the range of δ -values to be able to assign this rock either to bulk silicate ($\delta^{60}\text{Ni} = 0.05 \pm 0.05$) or ultramafic (-0.3 to $+0.2\%$).⁴⁵ To reduce the uncertainty of our measurement, more measurements would be required. Hence, and as stated earlier, a larger number of measurements is required to obtain a better accuracy. Similar effects are observed while analyzing the spectra and the intensity correlations of the B, Mg, and Ni isotopes of the dark inclusions. The $\delta^{11}\text{B}$ value we obtained in the studies show obvious fractionation in the sample, which is attributed to chemical transformation in the ancient ocean induced by the pH level of water.⁴⁸

Additional isobaric interferences to the Ni isotopes are to be expected from the MgO_2 , Si_2 , C_5 , and CaO compounds. The Mg, Si, C_5 , and Ca are abundant elements at the location of the micrometer inclusions and can form easily X_n clusters and X_nO_m oxides due to chemistry in the expanding plasma plume. The clusters of these elements can be identified readily in the SP mass spectra but are observed rarely in the DP mass spectra. Nevertheless, without instrumentation providing a sufficiently high mass resolving power, their presence or absence cannot be assessed with certainty. The results of the present studies on statistically relevant numbers of the measurements are shown in Figures 3, 6, and 9. The results are encouraging and improved by a factor of 10 comparing to the accuracies typically achieved with LIMS instruments.¹ The accuracy and precision achieved for a few measurements micrometer-sized inclusions in the aragonite host material is low, but the improvements are expected by conducting the measurements on larger number of samples.

The analysis method applied here relies on the presence of sufficiently high isotope mass peak intensities. The 100 or 200 single-shot accumulation for the analyzed spectrum of the individual ablation layer was a trade-off between the control of the spectra quality and achieving sufficiently high signal intensities. Ideally, single-shot mass spectra recording would be beneficial because spectra affected by space charge, sample surface charging, and plasma plume variabilities could be removed more efficiently. Nevertheless, for the analyses of such geological samples, with a variable number of elements at variable concentrations, the signal intensities of the element of interest can be very small. To enhance their S/N, it is necessary to accumulate a high enough number of spectra before analysis. Therefore, the effects deteriorating the spectra cannot be completely removed by the filtering method, but their contribution can be reduced. The requirements for the sufficiently intense isotope mass peaks constrain the application of this method to elements with sufficiently high abundant isotope components, for example, the concentration of the elements C and S in our samples is too low for a good isotope analysis. Moreover, the method works best when the

mass peaks intensities are not severely affected by interfering isobaric mass peak intensities.

5 | CONCLUSIONS

In this study, the isotope composition of the Ni isotopes in NIST SRM 986, the Mg and the Ni isotopes in the trevorite mineral, and B, Mg, and Ni isotopes in dark, micrometer-sized inclusions embedded in an aragonite host material have been investigated using our miniature LIMS system. The studies were conducted using both modes the DP ablation/ionization mode and in certain cases, for comparison the classic measurement scheme of single laser pulse. The application of the DP method allows to reduce abundances of cluster and molecular ions in the ablated ion beam and to increase the intensities of atomic ions. The measurements are conducted by applying the depth profiling measurement procedure. The ablated layers thicknesses are within a submicrometer depth resolution and the collected mass spectra reflect the chemical composition of each ablated layer.

For accurate isotope compositional analysis we present and apply measurement and data analyses methods based on filtering and correlation routines that allow a better understanding of interfering effects that limit isotope ratio measurements using our LIMS system. First, the spectra filtering method is applied to the recorded data that removes efficiently low quality mass spectra by means of, for example, mass resolution. Plasma variabilities, sample surface charging, and space charge effects are the main sources for poor spectra quality observed. Following the spectra filtering procedure, an isotope intensity correlation method is applied that allows the identification of suitable mass spectra for isotope ratio analysis, for example, spectra that show no detector saturation. After filtering, this correlation method is applied one more time to the remaining set of mass spectra for final isotope ratio analysis. Spectra from which the isotope intensities correlate linearly are accepted for the final isotope ratio analyses providing that the data points deviate no more than $\pm 2\sigma$ standard deviation from the values given by the trend line of the correlation. The intensity correlation method relies on the experimental observation that for certain accumulation number the isotope intensity variations are small. The laser ablation stability during the measurements results in highly correlated isotope mass peak intensity correlations. Applying this analysis method, we derived for the Ni isotope reference material a mean of $\delta^{60}\text{Ni} = 0.47 \pm 0.68$. For the trevorite mineral mean isotope ratio values of Mg and Ni of $\delta^{26}\text{Mg} = -0.13 \pm 0.96$ and $\delta^{60}\text{Ni} = -0.30 \pm 1.15$ could be derived. For B and Ni element isotopes investigated in the dark, micrometer inclusions, a mean value of $\delta^{11}\text{B} = -46.1 \pm 2.9$ and $\delta^{60}\text{Ni} = -3.3 \pm 0.8$ could be derived. Due to saturation effects only one single value for Mg could be measured, which is $\delta^{26}\text{Mg} = -4.5 \pm 8.0$.

The presented analysis method allows the identification of micrometer-sized inclusions in natural samples and the in situ isotope analysis at these locations, removing the need for complex sample extraction and preparation. Moreover, the method allows for the efficient elimination of measurement effects that limit the accuracy of

isotope ratio measurements based on a statistical approach using our miniature LIMS system. The filtering and correlation analysis method is simple and robust in its application, which makes it suitable for the integration for postprocessing analysis of mass spectrometric data collected of solids investigated in situ a planetary surface by our system. With the currently available improvements, the isotope accuracies will be likely to get some more insight to ancient ocean properties (B-isotopes), character of rocks (Ni-isotopes) and possible some insights into bio-signature (Ni-isotope), in addition to commonly applied C- and S-isotope biosignatures.

ACKNOWLEDGEMENTS

This work was supported by the Swiss National Science Foundation, the Swedish Research Council (contracts nos. 2012-4364, 2017-04129, and 2017-05018) and a Villum Investigator Grant to Don Canfield (No. 16518).

ORCID

Marek Tulej  <https://orcid.org/0000-0001-9823-6510>

Anna Neubeck  <https://orcid.org/0000-0002-1291-5529>

Andreas Riedo  <https://orcid.org/0000-0001-9007-5791>

Valentine Grimaudo  <https://orcid.org/0000-0002-7010-5903>

Niels F.W. Ligterink  <https://orcid.org/0000-0002-8385-9149>

Magnus Ivarsson  <https://orcid.org/0000-0002-4548-1560>

Wolfgang Bach  <https://orcid.org/0000-0002-3099-7142>

Coenraad de Koning  <https://orcid.org/0000-0002-2540-7689>

Peter Wurz  <https://orcid.org/0000-0002-2603-1169>

REFERENCES

1. Becker JS. State-of-the-art and progress in precise and accurate isotope ratio measurements by ICP-MS and LA-ICP-MS Plenary Lecture. *J Anal At Spectrom.* 2002;17(9):1172-1185.
2. Lin YM, Yu QA, Hang W, Huang BL. Progress of laser ionization mass spectrometry for elemental analysis—a review of the past decade. *Spectrochim Acta B.* 2010;65(11):871-883.
3. Riedo A, Bieler A, Neuland M, Tulej M, Wurz P. Performance evaluation of a miniature laser ablation time-of-flight mass spectrometer designed for in situ investigations in planetary space research. *J Mass Spectrom.* 2013;48(1):1-15.
4. Riedo A, Neuland M, Meyer S, Tulej M, Wurz P. Coupling of LMS with a fs-laser ablation ion source: elemental and isotope composition measurements. *J Anal Atom Spectrom.* 2013;28(8):1256-1269.
5. Zhang BC, He MH, Hang W, Huang BL. Minimizing matrix effect by femtosecond laser ablation and ionization in elemental determination. *Anal Chem.* 2013;85(9):4507-4511.
6. Russo RE, Mao X, Gonzalez JJ, Mao SS. Femtosecond laser ablation ICP-MS. *J Anal At Spectrom.* 2002;17(9):1072-1075.
7. He J, Huang RF, Yu Q, Hang W, Huang BL. Standardless semi-quantitative elemental analysis of steel using laser ablation time-of-flight mass spectrometry. *Chem J Chinese U.* 2009;30:57-59.
8. Appelblad PK, Rodushkin I, Baxter DC. Sources of uncertainty in isotope ratio measurements by inductively coupled plasma mass spectrometry. *Anal Chem.* 2001;73(13):2911-2919.
9. Rameback H, Berglund M, Vendelbo D, Wellum R, Taylor PDP. On the determination of the true dead-time of a pulse-counting system in isotope ratio mass spectrometry. *J Anal Atom Spectrom.* 2001;16(11):1271-1274.
10. Tulej M, Meyer S, Luthi M, et al. Detection efficiency of microchannel plates for e(−) and pi(−) in the momentum range from 17.5 to 345 MeV/c. *Rev Sci Instrum.* 2015;86(8):1-12, 083310.
11. Wiesendanger R, Grimaudo V, Tulej M, et al. The LMS-GT instrument—a new perspective for quantification with the LIMS-TOF measurement technique. *J Anal Atom Spectrom.* 2019;34(10):2061-2073.
12. Lin YM, Yu Q, Huang RF, Hang W, He J, Huang BL. Characterization of laser ablation and ionization in helium and argon: a comparative study by time-of-flight mass spectrometry. *Spectrochim Acta B.* 2009;64(11-12):1204-1211.
13. He MH, Li B, Yu SY, et al. Buffer-gas assisted high irradiance femtosecond laser ionization orthogonal time-of-flight mass spectrometry for rapid depth profiling. *J Anal Atom Spectrom.* 2013;28(4):499-504.
14. Tulej M, Wiesendanger R, Riedo A, Knopp G, Wurz P. Mass spectrometric analysis of the Mg plasma produced by double-pulse femtosecond laser irradiation. *J Anal Atom Spectrom.* 2018;33(8):1292-1303.
15. Managadze GG, Safronova AA, Luchnikov KA, et al. A new method and mass-spectrometric instrument for extraterrestrial microbial life detection using the elemental composition analyses of Martian regolith and permafrost/ice. *Astrobiology.* 2017;17(5):448-458.
16. Managadze GG, Wurz P, Sagdeev RZ, et al. Study of the main geochemical characteristics of Phobos' regolith using laser time-of-flight mass spectrometry. *Solar Syst Res+.* 2010;44(5):376-384.
17. Brinckerhoff WB, Managadze GG, McEntire RW, Cheng AF, Green WJ. Laser time-of-flight mass spectrometry for space. *Rev Sci Instrum.* 2000;71(2):536-545.
18. Anderson FS, Nowicki K, Whitaker T. In-situ Rb-Sr geochronology. Proceedings of the Aerospace Conference, 2013 IEEE. 2-9 March 2013, Big Sky, MT. ISBN: 978-1-4673-1812-9, id.204. <https://doi.org/10.1109/AERO.2013.6497158>
19. Rohner U, Whitby JA, Wurz P. A miniature laser ablation time-of-flight mass spectrometer for in situ planetary exploration. *Meas Sci Technol.* 2003;14(12):2159-2164.
20. Riedo A, Meyer S, Heredia B, et al. Highly accurate isotope composition measurements by a miniature laser ablation mass spectrometer designed for in situ investigations on planetary surfaces. *Planet Space Sci.* 2013;87:1-13.
21. Cameron V, Vance D, Archer C, House CH. A biomarker based on the stable isotopes of nickel. *Proc Natl Acad Sci U S A.* 2009;106(27):10944-10948.
22. Stephan T, Trappitsch R, Davis AM, et al. CHILI—the Chicago Instrument for Laser Ionization—a new tool for isotope measurements in cosmochemistry. *Int J Mass Spectrom.* 2016;407:1-15.
23. Grimaudo V, Moreno-Garcia P, Riedo A, et al. High-resolution chemical depth profiling of solid material using a miniature laser ablation/ionization mass spectrometer. *Anal Chem.* 2015;87(4):2037-2041.
24. Reid JD, Zhou J. Impact of leveler molecular weight and concentration on damascene copper electroplating. *ECS Trans.* 2007;2:77-92.
25. Lühn O, Van Hoof C, Ruythooren W, Celis JP. Filling of microvia with an aspect ratio of 5 by copper electrodeposition. *Electrochim Acta.* 2009;54(9):2504-2508.
26. Qian G, Li Y, Gerson AR. Applications of surface analytical techniques in Earth Sciences. *Surf Sci Rep.* 2015;70(1):86-133.
27. Kelly CJ, McFarlane CRM, Schneider DA, Jackson SE. Dating micrometre-thin rims using a LA-ICP-MS depth profiling technique on zircon from an Archaean Metasediment: comparison with the SIMS depth profiling method. *Geostand Geoanal Res.* 2014;38(4):389-407.
28. Tulej M, Neubeck A, Ivarsson M, et al. Chemical composition of micrometer-sized filaments in an aragonite host by a miniature laser ablation/ionization mass spectrometer. *Astrobiology.* 2015;15(8):669-682.
29. Neubeck A, Tulej M, Ivarsson M, et al. Mineralogical determination in situ of a highly heterogeneous material using a miniaturized laser

- ablation mass spectrometer with high spatial resolution. *Int J Astrobiol.* 2016;15(2):133-146.
30. Neubeck A, Tulej M, Wiessendanger R, et al. Laser ablation ionization mass spectrometer analyses of stable Ni isotope fractionation in fossilized microstromatolites. *Nature.* 2020. submitted, 1-13.
 31. Tzamos E, Filippidis A, Rassios A, et al. Major and minor element geochemistry of chromite from the Xerolivado-Skoumtsa mine. *J Geochem Explor.* 2016;165:81-93.
 32. Bach W, Rosner M, Jons N, et al. Carbonate veins trace seawater circulation during exhumation and uplift of mantle rock: results from ODP Leg 209. *Earth Planet Sc Lett.* 2011;311(3-4):242-252.
 33. Riedo A, Tulej M, Rohner U, Wurz P. High-speed microstrip multi-anode multichannel plate detector system. *Rev Sci Instrum.* 2017; 88(4):1-6, 045114.
 34. Wiesendanger R, Wacey D, Tulej M, et al. Chemical and optical identification of micrometer-sized 1.9 billion-year-old fossils by combining a miniature laser ablation ionization mass spectrometry system with an optical microscope. *Astrobiology.* 2018;18(8):1071-1080.
 35. Grimaudo V, Moreno-Garcia P, Lopez AC, et al. Depth profiling and cross-sectional laser ablation ionization mass spectrometry studies of through-silicon-vias. *Anal Chem.* 2018;90(8):5179-5186.
 36. Meyer S, Riedo A, Neuland MB, Tulej M, Wurz P. Fully automatic and precise data analysis developed for time-of-flight mass spectrometry. *J Mass Spectrom.* 2017;52(9):580-590.
 37. Wiesendanger R, Tulej M, Grimaudo V, et al. A method for improvement of mass resolution and isotope accuracy for laser ablation time-of-flight mass spectrometers. *J Chemometr.* 2018;1-10.
 38. Grimaudo V, Moreno-Garcia P, Lopez AC, et al. Combining anisotropic etching and PDMS casting for three-dimensional analysis of laser ablation processes. *Anal Chem.* 2018;90(4):2692-2700.
 39. Grimaudo V, Moreno-Garcia P, Riedo A, et al. Review-laser ablation ionization mass spectrometry (LIMS) for analysis of electrodeposited Cu interconnects. *J Electrochem Soc.* 2018;166:D3190-D3199.
 40. Becker JS. *Inorganic Mass Spectrometry: Principles and Applications.* John Wiley & Sons; 2007. ISBN: 978-0-470-51720-8.
 41. Tulej M, Riedo A, Neuland MB, et al. CAMAM: a miniature laser ablation ionisation mass spectrometer and microscope-camera system for in situ investigation of the composition and morphology of extraterrestrial materials. *Geostand Geoanal Res.* 2014;38(4):441-466.
 42. Neuland MB, Grimaudo V, Mezger K, et al. Quantitative measurement of the chemical composition of geological standards with a miniature laser ablation/ionization mass spectrometer designed for in situ application in space research. *Meas Sci Technol.* 2016;27(3): 1-13, 035904.
 43. Meija J, Coplen TB, Berglund M, et al. Isotopic compositions of the elements 2013 (IUPAC Technical Report). *Pure Appl Chem.* 2016; 88(3):293-306.
 44. Kakegawa T, Noda M, Nannri H. Geochemical cycles of bio-essential elements on the early earth and their relationships to origin of life. *Resour Geol.* 2002;52(2):83-89.
 45. Buettnner KM, Valentine AM. Bioinorganic chemistry of titanium. *Chem Rev.* 2012;112(3):1863-1881.
 46. Turekian KK. The marine geochemistry of strontium. *Geochim Cosmochim Acta.* 1964;28(9):1479-1496.
 47. Masuda H. Arsenic cycling in the Earth's crust and hydrosphere: interaction between naturally occurring arsenic and human activities. *Prog Earth Planet Sci.* 2018;5(68):1-11.
 48. Kaczmarek K, Langer G, Nehrke G, et al. Boron incorporation in the foraminifer *Amphistegina lessonii* under a decoupled carbonate chemistry. *Biogeosciences.* 2015;12(6):1753-1763.
 49. Grimaudo V, Moreno-Garcia P, Riedo A, et al. Toward three-dimensional chemical imaging of ternary Cu-Sn-Pb alloys using femto-second laser ablation/ionization mass spectrometry. *Anal Chem.* 2017;89(3):1632-1641.

How to cite this article: Tulej M, Neubeck A, Riedo A, et al. Isotope abundance ratio measurements using femtosecond laser ablation ionization mass spectrometry. *J Mass Spectrom.* 2020;55:e4660. <https://doi.org/10.1002/jms.4660>